Chemical Engineering Journal xxx (xxxx) xxx–xxx

Contents lists available at ScienceDirect

Chemical Engineering Journal

journal homepage: www.elsevier.com/locate/cej

Fluidized bed reactor assisted by Oxygen Transport Membranes: Numerical simulation and experimental hydrodynamic study

Tania Antonini[a], Andrea Di Carlo[a], Pier Ugo Foscolo[a], Katia Gallucci[a,*], Stefano Stendardo[b]

[a] Industrial Engineering Department, University of L'Aquila, Via G. Gronchi, 18-67100 L'Aquila, Italy
[b] ENEA, Casaccia Research Centre, 00100 Roma, Italy

HIGHLIGHTS

- Application of Oxygen Transport Membrane (OTM) technology.
- Hydrodynamic cold model study of a fluidized bed reactor with internals.
- Simulation of methane oxy-combustion and calcium carbonate calcination.

ARTICLE INFO

Keywords:
Fluidized bed
Cold model with internals
OTM
CaO-based sorbent
Numerical simulation

ABSTRACT

In the near future, H_2 is bound to become an important energy carrier used for surplus power storage and for sustainable transportation. An innovative technology for the production of a H_2 rich gas is the Sorption Enhanced Reforming (SER) of hydrocarbons: a solid CaO-based sorbent is used to capture CO_2 produced by reforming and water gas shift, enhancing the equilibrium. $CaCO_3$ is decomposed in a fluidized bed oxy-combustion calciner and the sorbent recycled. In this work, the interest is focused on the Calcium Looping (CaL) cycle, more specifically on the combustor/calciner fluidized bed reactor of the pilot scale platform ZECOMIX (ENEA – 5 kmol/h of H_2). The feasibility to feed O_2 to a bubbling fluidized bed calciner by means of Oxygen Transport Membranes (OTM) is studied using a simulation model. The fluidizing flow rate is made of CO_2 and CH_4, preliminarily heated up to 700–850 °C by heat exchange with the output gas stream (above 900 °C); overall gas flow rate and methane content are enough to reach vigorous bubbling fluidization ($u \approx 10\, u_{mf}$) and temperature required by calcination, respectively. Cold model experimental tests with a cylindrical bubbling fluidized bed reactor with internals (vertical rods mimicking the OTM system) are carried out to support the design of the calciner unit in the ZECOMIX experimental platform. The hydrodynamic study is performed under ambient conditions to simulate fluidized bed expansion and to evaluate bubbles behavior in the calciner, in presence of vertical, tubular membranes for oxygen transfer.

1. Introduction

The abundance of natural gas at low cost, made available by innovative extraction techniques, accompanies the transition to a low carbon economy. Natural gas is characterized by a chemical composition rich in hydrogen and relatively scarce in carbon content, so that when its utilization replaces coal or oil, the carbon dioxide accumulation rate in the atmosphere is substantially reduced [1–5]. Renewable energy sources and increased efficiency in energy utilization will certainly characterize the economic development and allow a more even distribution of resources [6–8], however the worldwide improvement in standards of life requires additional energy consumption so that in the coming decades we should still rely on an important contribution of fossil resources [9].

Steam reforming of natural gas is the most popular route to produce hydrogen, not available in nature as H_2, the use of which is expected to expand from today important feedstock in different chemical processes to a widespread energy vector for power generation and transportation, especially in highly populated areas, those most exposed to the noxious effects of air pollution [10].

Steam Methane Reforming (SMR), and reforming of hydrocarbons in general, is a mature catalytic process, deeply studied and widely applied industrially [11], however still amenable to important improvements aiming at milder reaction conditions and higher hydrogen

* Corresponding author.
E-mail address: katia.gallucci@univaq.it (K. Gallucci).

https://doi.org/10.1016/j.cej.2018.11.021

Notation

Abbreviations

ASU	Air Separation Unit
CBN	Carbonation
CFD	Computational Fluid Dynamics
DAGF	Dispersive Axial Gas Flow
MIEC	Mixed Ionic and Electronic Conducting
OTM	Oxygen Transport Membrane
PGM	Particle Grain Model
RTD	Residence Time Distribution
SESMR	Sorption Enhanced Steam Methane Reforming
SMR	Steam Methane Reforming
TGA	Thermo-gravimetric Analyzer
WGS	Water Gas Shift

Symbols

$c_{p,g}$	Gas specific heat capacity, J/mol/°C
$c_{p,s}$	Solid specific heat capacity, J/kg/°C
C_i	Molar concentration of species i, mol/m^3
d_B	Bubble diameter, m
d_{calci}	Calciner diameter, m
d_m	OTM average diameter, m
d_p	Particle diameter, m
D_R	Axial dispersion coefficient, m^2/s
F	Molar flow rate, mol/s
h	Heat transfer coefficient, W/m^2/°C
H	Height, m
J_{O2}	O_2 permeation flux, mol/m^2/s
k_g	Gas mass transfer coefficient, m/s
k_r	Reverse surface exchange rate constant, mol/m^2/s
K_{be}	Bubble-to-emulsion phase mass transfer coefficient, m/s
N	OTM pipe number, dimensionless
N_{CaO}	Moles per unit volume of sorbent particle, mol/m^3
P	Pressure, atm
$Pitch$	Spacing among tubular OTM/rods, m
$P_{O2,I}$	O_2 partial pressure on the permeate side, atm
$P_{O2,air}$	O_2 partial pressure on the air side, atm
Q	Volumetric gas flow rate, m^3/s
$\boldsymbol{r_{calci}}$	Rate of calcination reaction, mol/m^3/s
$\boldsymbol{r_{CBN}}$	Rate of carbonation reaction, mol/m^3/s
R	Ideal gas constant, J/mol/K
S	Cross section, m^2
t	Time, s
T	Temperature, K
u_{mf}	Minimum fluidization velocity, m/s
u_p	Solid phase rising velocity, m/s
V_{bed}	Calciner bed volume, m^3
V_{CaO}	Molar volume of CaO, m^3/kmol
V_{CaCO3}	Molar volume of $CaCO_3$, m^3/kmol
W_s	Solid flow rate, kg/s
X	Carbonation conversion, dimensionless
X_{calci}	Calcination conversion/degree, dimensionless
z	Axial coordinate
Z	Ratio between molar volumes of $CaCO_3$ and CaO, dimensionless

Dimensionless numbers

Ar	Archimedes number (defined in Table 3)
De	Density number (defined in Table 3)
Fl	Flow number (defined in Table 3)
Le	Length number (defined in Table 3)
Pe	Péclet number ($u\ H/D_R$)

Greek letters

β	Molar ratio between CO and CO_2 [38], dimensionless
ρ	Density, kg/m^3
μ	Viscosity, Pa·s
δ	Bubble volume fraction, dimensionless
ν	Stoichiometric coefficient, dimensionless
ε	Bed voidage, dimensionless

Subscripts and superscripts

out	Output
av	Average
b	Bubble
e	Emulsion
eq	Equilibrium
g	Gas phase
s	Solid phase
0	Initial condition
mf	Minimum fluidization
p	Particle
P	Probe

yield with a reduced number of plant equipment, which in general terms is often called process intensification [12].

In order to enhance the equilibrium of the reforming reaction according to the *Le Chatelier* principle, addition of calcium oxide sorbents for CO_2 capture to nickel catalyst in the reformer reactor has been demonstrated to be feasible from the point of view of compatibility between the reforming and the sorption processes as far as temperature level is concerned [13,14], and of thermal integration between endothermic and exothermic reactions:

$$SMR \quad CH_4 + H_2O \leftrightarrow 3H_2 + CO \qquad \Delta H^0_{298} = +206 kJ/mol \qquad (1)$$

$$WGS \quad CO + H_2O \leftrightarrow H_2 + CO_2 \qquad \Delta H^0_{298} = -41 kJ/mol \qquad (2)$$

$$CBN \quad CaO + CO_2 \rightarrow CaCO_3 \qquad \Delta H^0_{298} = -178 kJ/mol \qquad (3)$$

The utilization of fluidized bed reactors for Sorption Enhanced Reforming (SER) would ensure steady state operation by circulation of the bed material between reformer and regenerator [15,16]. Demonstration units were operated successfully and mass and energy balances for different options of process flow sheet for industrial installations were studied to assess technical and economic feasibility [17–19].

Intrinsic aspects concerning simultaneous catalytic reforming and CO_2 sorption reaction processes were also investigated, at different levels: preparation and characterization of synthetic CaO-based sorbents with sufficient capacity, sorption rate and stability over repeated sorbent-regeneration cycles, preparation and characterization of hybrid sorbent-catalyst materials, particle attrition resistance in the fluidized bed environment, multi-scale models at the level of single particle and lab scale packed bed reactors, Computational Fluid Dynamic (CFD) approaches to simulate accurately the fluidized bed reformer [14,20–25].

Less attention was payed to sorbent regeneration, i.e. calcium carbonate calcination, which is needed to recycle fresh sorbent to the SER reactor, by means of a solid circulation loop, and allow steady state operation [26]. In the whole process, however, sorbent regeneration is the conversion step that requires the highest temperature level: in order to obtain pure CO_2 amenable to utilization and/or storage, about 900 °C

are required at ambient pressure to allow a favorable carbon dioxide concentration gap (driving force) with reference to equilibrium conditions [27]; moreover, being the calcination process endothermic, heat should be supplied to the calciner at these high temperature conditions.

The last aspect is particularly challenging, when considering both investment and operating costs, and the overall requirement of energy efficiency: as a matter of fact, different options have been studied to provide the necessary input of heat, spanning from indirect heat supply utilizing the anode waste stream from a solid oxide fuel cell coupled to the reformer, through a bundle of heat exchange pipes resistant to temperature as high as 1000 °C, immersed inside the particulate bed of the calciner, to direct heating by means of oxy-combustion of a gaseous fuel (methane), in order to avoid dilution with nitrogen of the CO_2 output [28]. The latter option appears more efficient and easier to be realized in practical cases, however the availability of a feeding stream of pure oxygen is required, with a noticeable increase of costs. This is especially true in the case of small to medium size installations, where an Air Separation Unit (ASU) would be difficult to integrate in the whole plant [17].

The innovation investigated in this work consists in the use of high temperature Oxygen Transfer Membranes (OTM) to provide the necessary input of oxygen. Their permeability increases with an exponential function of temperature and reaches appreciable values just at the operating conditions of the calciner; in addition, pressurization of the air feed on the retentate side of the membrane is not needed, because the permeation mechanism is governed by the difference of electrochemical potential and is based on the diffusion of oxygen anions and electrons across the membrane body in opposite directions [29].

The feasibility to provide enough oxygen to a bubbling fluidized bed calciner by means of OTM is studied with a simulation model, with reference to the pilot scale platform ZECOMIX for applied research on hydrogen production and utilization run by ENEA (Italian National Agency for New Technologies, Energy and Sustainable Economic Development). In the case examined, a gas micro-turbine (100 kW) is tested with hydrogen feed produced in a SER system that supplies 5 kmol/h of this fuel; a natural sorbent is utilized: calcined dolomite [30,31].

To our knowledge, despite industrial interest for the development of OTM technology and its great potential for oxygen separation from air at high temperature, realization of a calciner prototype of significant size including tubular OTMs is not yet easily feasible [32], therefore a direct validation of the global mathematical model would be difficult/impossible. It should be considered, however, that the model proposed here is obtained assembling together different sub-models, all of them validated by means of experimental measures:

- The fluid dynamic behavior of the fluidized bed calciner is characterized by operating a so called “cold model”, geometrically and dynamically similar, i.e. assuring faithful correspondence of bubble flow, size, volume fraction inside the bed, etc.: such a procedure is quite well established and adopted since long time [33];
- Gas mixing phenomena along the bed are quantified by axial dispersion, the intensity of which has been measured experimentally on the “cold model” by determination of residence time distribution of an inert tracer gas;
- As far as sorbent calcination is concerned, an experimentally validated dynamic model proposed in the literature [34] was further checked and adapted by means of data purposely obtained with TGA tests;
- As far as CaO-based sorbent carbonation is concerned, the reaction rate under different conditions was deeply studied experimentally, as well as with model developments, in previous works of this group (for example [35]);
- OTM permeability data in the relevant temperature range were previously collected in our laboratory utilizing a tubular sample of OTM, of the same type, diameter and thickness of that proposed for the prototype calciner, assembled in exactly the same mode as shown in Fig. 1b. They allowed defining values of the parameters appearing in the oxygen transfer rate expression, and calculating oxygen flux as a function of temperature.

2. Calcination process and closure equations relevant to the model

As mentioned above, among likely calciner configurations [36], a solid transport reactor with fuel oxy-combustion directly in the fluidized bed is considered here (Fig. 1a), and its feasibility is investigated; the feeding gas stream is made of carbon dioxide and methane, preliminarily heated up to 700–850 °C by heat exchange with the hot output gas stream (above 900 °C); flow rate and methane content are

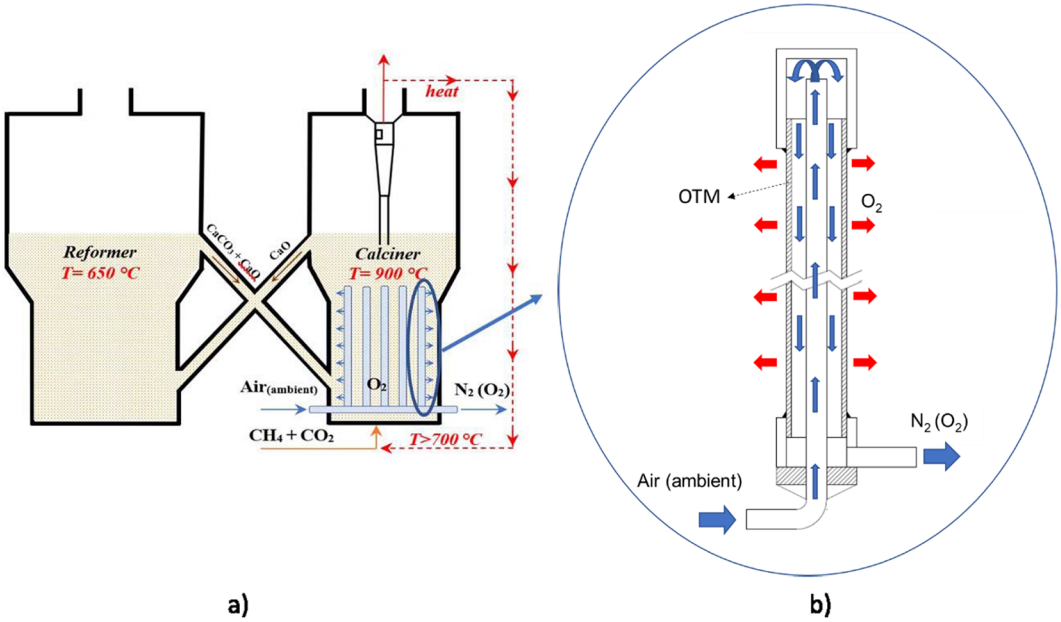

Fig. 1. a) Conceptual scheme of the Calcium Looping (CaL) process system for CO_2 capture assisted by Oxygen Transport Membranes; b) Arrangement of a single tubular membrane and related fittings, with input air, retentate and oxygen flows.

enough to reach vigorous bubbling fluidization ($u \approx 10u_{mf}$) and temperature conditions ($T \approx 900\ ^{\circ}C$) required by calcination, respectively. Fig. 1b shows with some details the arrangement of a single tubular membrane and related fittings, with input air, retentate and oxygen flows. Differential thermal dilatation between membranes and fitting pipes is the main reason why this arrangement was chosen and checked experimentally in a previous work [37].

2.1. Rate of oxygen transfer

Oxygen is fed progressively by means of a vertical bundle of tubular Oxygen Transport Membranes (OTM) immersed in the fluidized bed, with air inner flow. Mixed Ionic and Electronic Conducting (MIEC) perovskite membranes show oxygen perm-selectivity at high temperature (usually $> 700\ ^{\circ}C$) with a permeation flux, J_{O2}, well described by an Arrhenius-type law; it is not needed to pressurize the air feeding stream [29,37]:

$$J_{O2} = k_g\,(P_{O2,air} - P_{O2,I})/RT = (d_{m,out}/d_{m,av})\cdot k_r\,[mol/cm^2/s] \tag{4}$$

$$k_r = 0.488\cdot exp\,[-13021/T]\,[mol/cm^2/s] \tag{5}$$

The above transfer rate equation is noticeably simplified by the assumption that, as soon as oxygen permeates through the membrane into the fluidized bed, methane burns instantaneously at the relatively high temperature existing there, according to the following stoichiometric equation, expressed in terms of one oxygen mole that permeates through the OTM surface:

$$O_2 + \frac{2(\beta+1)}{3\beta+4}CH_4 \rightarrow \frac{2\beta}{3\beta+4}CO + \frac{2}{3\beta+4}CO_2 + \frac{4(\beta+1)}{3\beta+4}H_2O \tag{6}$$

where the ratio between CO and CO_2 produced by methane combustion, β, is given by [38] as a function of temperature:

$$\beta = 10^{3.4}\cdot exp\,[-12400/1.98/T] \tag{7}$$

Such perovskite hollow fiber membranes are potentially able to provide a pure oxygen feed to the calciner, avoiding an energy intensive Air Separation Unit (ASU) [39], although their mechanical stability still needs to be optimized.

2.2. Rate of dolomite calcination and carbonation

An upward moving bed of particulate solids is established in the calciner: the exhaust sorbent, or sorbent/catalyst, material withdrawn from the reformer is fed just above the gas distributor at about 650 °C, while the calcined material overflows at the bed surface and is fed back to the reformer; its heat content helps operating the SER reactor in adiabatic mode (see Fig. 1a). Loop seals on the solid transfer lines help controlling the sorbent circulation rate and gas leakages between both reactors. The inlet solid mass flow rate to the calciner is fixed according to gas decarbonation requirements of the whole process and sorbent capture capacity.

To develop a realistic model of the calciner and obtain numerical predictions of its behavior, Pilkington dolomite is assumed to be the CO_2 sorbent, with physical and chemical properties reported in Table 1.

In order to obtain a CO_2 stream of relatively high purity, $CaCO_3$ should be calcined in a CO_2 rich atmosphere; according to the thermodynamic equilibrium between CaO and gaseous CO_2 [27], the calcination temperature increases with increasing CO_2 partial pressure (Fig. 2).

A calcination test with a fresh dolomite sample was carried out in a Linseis STA PT 1000 Thermogravimetric Analyzer (TGA) equipped with a gas flow rate dynamic control system (L40/2053), to study the dynamic behavior of this natural CaO-based CO_2 sorbent, under conditions similar to those assumed for the calciner reactor.

In this TGA test, Pilkington dolomite particles with average diameter 500 μm were used as solid material.

The temperature profile consists of a first calcination step at 925 °C of 30 min after a heating ramp of 10 °C/min, followed by a cooling step at 30 °C, always under a N_2 atmosphere: this procedure assures a complete calcination of dolomite. The carbonation step, at 650 °C for 30 min, and a second calcination at 925 °C for 180 min were performed under a gas composition of CO_2/N_2 equal to 80/20 % by volume, while the heating ramp at 10 °C/min between these phases was carried out under pure CO_2 atmosphere.

The experimental calcination conversion of dolomite *vs* time, under severe regeneration conditions, is shown in Fig. 3.

According to the kinetic model proposed by Fang et al. [34]:

$$\frac{dX_{calci}}{dt} = k_{0calci}\,e^{-E_{calci}/RT}(1 - X_{calci})^{2/3}(C_{CO2,eq} - C_{CO2}); \quad C_{CO2,eq} > C_{CO2} \tag{8}$$

the predicted $CaCO_3$ calcination curve, also shown in Fig. 3, fits satisfactorily the experimental results when the pre-exponential factor, k_{0calci}, in the kinetic constant is assumed equal to 18000 m^3/mol/s. In their work with a different type of dolomite under similar operating conditions, a higher value was proposed, k_{0calci} = 23797 m^3/mol/s, although of the same order of magnitude, denoting a somewhat faster calcination rate in that case. The activation energy term in Eq. (8), E_{calci}/R, is equal to 18041 K, as proposed in [34].

As a result, the chemical reaction rate for the calcination process is:

$$\boldsymbol{r_{calci}} = N_{CaO}\cdot dX_{calci}/dt \ \ [mol/m^3/s] \tag{9}$$

It should be also considered here that the partially carbonated sorbent is fed at the bottom of the calciner, where the temperature level is below that required for calcination; therefore, it is expected that some additional carbonation takes place there, in presence of a gaseous phase rich in carbon dioxide, before reaching the temperature level required for calcination at those conditions. This might appear as an adverse event; however, as it will become evident by results of simulations, the heat produced by exothermic carbonation will contribute to enhance the temperature profile and membrane permeability at the bottom of the reactor: as a result of this virtuous circle, complete calcination is achieved over a comparatively lower bed height than that required when the additional source of endogenous heat provided by sorbent further carbonation is absent; on the other hand, the methane input needed to supply thermal energy to the calciner is kept the same in both cases.

In previous studies [35,40,41], the carbonation process was deeply investigated and a satisfactory Particle Grain Model (PGM) developed and validated; according to these papers, the rate of carbonation, $\boldsymbol{r_{CBN}}$, can be expressed as follows:

$$\boldsymbol{r_{CBN}} = N_{CaO}\frac{dX}{dt} = \frac{N_{CaO}\frac{6V_{CaO}}{\delta_{CaO}}k_{CBN}(1-X)^{2/3}(C_{CO_2} - C_{CO_2,eq})}{1 + \frac{k_{CBN}}{2D_{PL}}\delta_{CaO}\sqrt[3]{1-X}\left(1 - \sqrt[3]{\frac{1-X}{1-X+X\cdot Z}}\right)} \ [mol/m^3/s]; \quad C_{CO_2} \geq C_{CO_2,eq} \tag{10}$$

where:

$$k_{CBN} = k_S\cdot N_{CaO} \tag{11}$$

Table 1
Physical and chemical properties of Pilkington dolomite [40].

Parameters		Values
CaO	[%, weight]	55.1
MgO	[%, weight]	44.9
N_{CaO}	[kmol/m^3]	12.7
Z	[-]	2.18
ε_{p0}	[-]	0.62
$\varepsilon_{pMgCO3\text{-}CaCO3}$	[-]	0.13
$\rho_{p,calci}$	[kg/m^3]	1307
d_p	[μm]	500

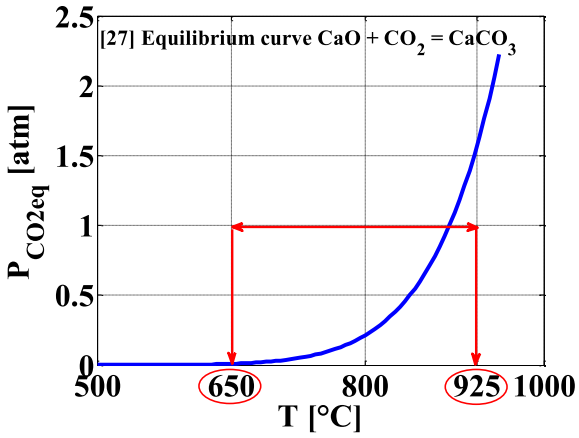

Fig. 2. Equilibrium curve for the reaction of CO_2 with CaO. Red lines represent the temperature jump from the solid carbonation step (SER reactor) to the calcination conditions needed to obtain pure gaseous CO_2 at atmospheric pressure.

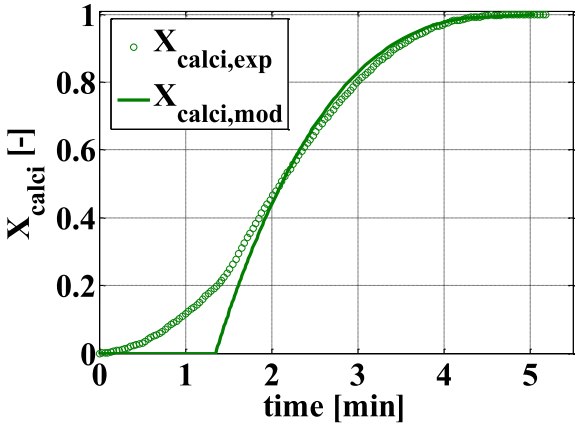

Fig. 3. Conversion of $CaCO_3$ to CaO *vs* time: experimental data under severe regeneration conditions and numerical predictions by Fang et al. [34] model with modified kinetic constant.

$$D_{PL}(X) = D_{PL,0} \cdot exp(-a \cdot X^b) \quad (12)$$

Parameter values applicable to the dolomite sample considered here are reported in Table 2.

The relation existing between carbonation conversion, X, and calcination degree is straightforward:

$$X_{calci} = 1 - X \quad (13)$$

3. Cold modelling hydrodynamic study

In order to study the fluidization quality and to support the design of an OTM-assisted fluidized bed calciner to be integrated in the ZECOMIX experimental platform, a hydrodynamic study was carried out at room temperature realizing a cold model made of a cylindrical, transparent column with internals (vertical rods mimicking the spatial hindrance of tubular OTM). The objective was to verify the influence of the internals on the bubble flow and the overall residence time distribution of the gas phase.

Fig. 4 shows the cold model layout; air at room temperature (1) was chosen as fluidization agent, and olivine was selected as bed material. The experimental rig is equipped with a rotameters bench for air flow measurement and control, varying from 9.30 to 513 l/min (2). Based on the design specifications of the hot facility, and according to dynamic similarity criteria for fluidization quality [43], the geometric characteristics and operating conditions for the cold model were properly fixed (Table 3).

Olivine (ρ_p = 2800 kg/m^3; d_p = 174 μm) and dolomite (ρ_p = 1307 kg/m^3; d_p = 500 μm) are both *Geldart* Group B powders [44], when fluidized by ambient air. The generalization of the *Geldart* classification in terms of the dimensionless numbers mentioned in Table 3, *Ar* and *De*, allows to obtain a corresponding map for fluidization by any fluid, at different temperature and pressure levels, as reported by [45]: olivine and dolomite particles selected for this dynamic similarity study, under the respective operating conditions are represented by practically coincident points on this map, and both fall into the Group B powders zone, i.e. they behave according to the bubbling regime as soon as they are fluidized.

The cylindrical column shown in Fig. 4, with internal diameter of 144 mm, is made in Plexiglas and a vertical tube bundle made of 136 rods, each 500 mm long and 3 mm in diameter, is housed inside the fluidized bed of olivine particles (3). The rods are assembled with a quadratic pitch and kept in position by means of two horizontal tube spacers. A pressure probe (4), can be moved vertically and is placed at different bed height during the experimental tests; it is connected to a Kistler piezoelectric transducer for the analysis of dynamic pressure fluctuations (5). It is worth noticing here that, according to the results obtained and illustrated below, the *Le* dimensionless number written in terms of the ratio between particle average diameter and the rods pitch size is more significant than that referred to the column diameter. As a matter of fact, for operational constraints the column diameter in the cold model is limited to 144 mm, although it should have been equal to 200 mm to agree closely with the geometric similarity rule: however, the overall outer surface area of the rods immersed in the fluidized bed is three times that of the column wall, and results of cold model tests (Fig. 5) show clearly the dominant effect of rods pitch on bubble size and flow pattern inside the bed.

The ratio between the horizontal spacing among OTM pipes (vertical rods in the cold model) immersed in the bed and the particle diameter is well above 10, assuring free movement of the fluidized particles in both systems and reliable extension to the calciner hydrodynamic conditions of dynamic pressure fluctuations, bed expansion and bubble properties measured with the cold model.

These experimental investigations did show that the vertical bundle immersed inside the bed plays a fundamental role to define the order of magnitude of horizontal bubble size, as shown in Fig. 5. The amplitude of dynamic pressure fluctuation is substantially reduced by the presence of rods: Fig. 5a compares results obtained with and without internals, at otherwise similar operating conditions; this result is confirmed by the corresponding trend of the standard deviation of the pressure signal as a function of fluidization velocity, measured at different bed heights (Fig. 5b) and by visual observations of the horizontal size of bubbles erupting at the bed surface, recorded with the help of a video camera (Fig. 5c). Fig. 5d shows a picture of bubbles rising through the bed of particles, close to the Plexiglas lateral wall: this picture indicates that

Table 2
Model parameter values for carbonation reaction.

Calcium oxide grain diameter, δ_{CaO} [40]	[nm]	150
Intrinsic carbonation rate constant, *ks* [42]	[m^4/kmol/s]	$5.95 \cdot 10^{-7}$
Initial value of product layer diffusion coefficient, $D_{PL,0}$ [40]	[m^2/s]	$2.0 \cdot 10^{-5}$
a (parameter in the expression of D_{PL}) [40]	[-]	36.8
b (parameter in the expression of D_{PL}) [40]	[-]	2

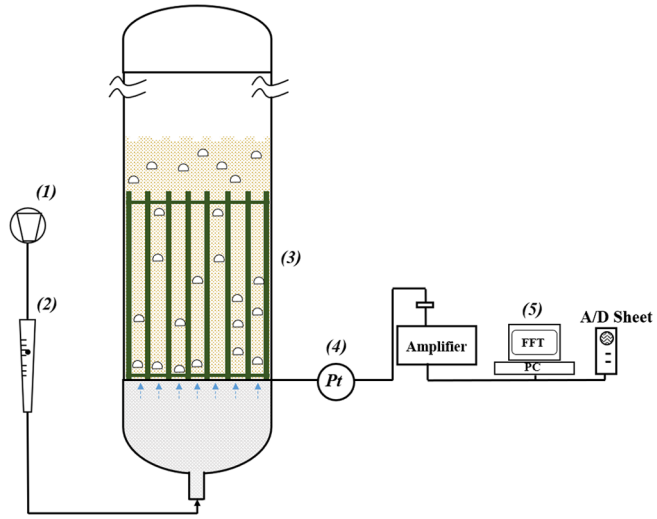

Fig. 4. Cold model layout of a cylindrical bubbling fluidized bed with internals.

Table 3
Geometric characteristics and operating conditions of the calciner reactor and of its dynamically similar cold model.

	Calciner (T ≈ 900 °C, P = 1 bar)	Cold Model (T = 20 °C, P = 1 bar)
ρ_g (kg/m^3)	0.46	1.1
μ $(Pa{\cdot}s)$	$4.4{\cdot}10^{-5}$	$1.8{\cdot}10^{-5}$
ρ_p (kg/m^3)	1307	2800
d_p (μm)	500	174
D_{column} (mm)	600	144
$OD\ tubular\ OTM/rods$ (mm)	10.0	3.0
$Pitch\ size$ (mm)	28.9	10.0
u_{mf} (m/s)	0.06	0.04
$Ar = \frac{d_p^3 \rho_p (\rho_p - \rho_g) g}{\mu^2}$	$1.10{\cdot}10^{6}$	$1.25{\cdot}10^{6}$
$De = \frac{\rho}{\rho_p}$	$3.5{\cdot}10^{-4}$	$3.9{\cdot}10^{-4}$
$Fl = \frac{u_0}{u_{mf}}$	11	10
$Le = \frac{L}{d_p}\left(\frac{Pitch}{d_p}\right)$	58	57

bubbles are rather elongated, and their horizontal size is of the same order of the pitch free section. Finally, the comparison between Fig. 5eI and eII shows that, other things being equal, the expanded fluidized bed height is higher when rods are absent: so, the bubble hold-up is bigger in this case, indicating a slower bubble rising velocity. As a result, it is possible to conclude that with vertical rods bubbles are much smaller and faster than those observed in the corresponding particulate bed empty of rods, in agreement with comprehensive studies on bubbling fluidized beds with vertical membranes [46].

Additional pulse input and step tracer tests with the cold model helped characterizing the distribution of gas residence times and making a reasonable assumption for the fluid dynamic behavior of the gas phase flowing through the fluidized bed. Concentration perturbations in the inlet stream were realized by adding carbon dioxide to the fluidizing air flow rate; CO_2 concentration as a function of time was detected in the outlet stream by means of a gas sampling probe located just above the fluidized bed, a sucking fan and an ABB online analyzer. Pulse and step tracer tests provided congruent characterization of gas Residence Time Distribution (RTD). In Fig. 6, results obtained with a pulse input are reported in dimensionless form, for different fluidizing velocities. At $u/u_{mf} = 10$, the relevant superficial velocity for simulation of the calciner, the first and second moment of RTD were evaluated and the axial Péclet number estimated.

4. Simulation model

Molar and energy balances for the calciner reactor were written according to a Dispersive Axial Gas Flow (DAGF) approach, with the assumption that the input flow rate, $Q_{tot,0}$, is divided between bubble and emulsion phase according to the two-phase theory of fluidization [45] applied here to a *Geldart* Group B particles system:

$$Q_{tot,0} = Q_{b,0} + Q_{e,0}; \qquad Q_{e,0}/S_{bed} = u_{mf} + u_p \varepsilon_{mf}; \qquad u_p = W_{s,0}/(\rho_{p,0} \cdot S_{bed}) \tag{14}$$

Carbon dioxide generated by calcination of the solid phase determines a progressive increase of bubble flow along the bed height, because of the onset of endogenous bubbles. This phenomenon resembles that accompanying devolatilization of biomass fuel particles immersed in a fluidized bed [47,48], although in this case it contributes favorably to the upward movement of the whole bed of progressively calcined (and then less dense) particles.

On the other hand, the relatively small change of molar flow due to carbon oxides and steam formation, when methane burns instantaneously with oxygen as soon as this permeates through the tubular membranes (see Eqs. (4)–(5)), is accommodated both in the bubbles and in the emulsion, according to the stoichiometric coefficients shown above and the volume fraction of the respective phase within the bed, δ and $(1\text{-}\delta)$, which in turn allows evaluating the amount of OTM surface in contact with bubbles and emulsion phase, respectively. The bubble fraction inside the bed is estimated from cold model tests at different superficial velocities: the following expression was obtained by interpolation of the experimental measurements of bed expansion as a function of the fluidizing velocity:

$$\delta = 0.012\frac{u}{u_{mf}} + 0.11; \qquad u > u_{mf} \tag{15}$$

In the calciner, temperature and molar flow rate both increase progressively along the bed height and so does the gas superficial velocity, u: therefore, the bubble volumetric fraction, δ, is also considered to increase as a function of u.

Table 4 summarizes the main input parameters utilized in simulations. The particulate solid is supposed to enter the calciner at the temperature of the SESMR reactor (650 °C) and with a carbonation degree, X, equal to 70 %, so to assure a good compromise between carbonation capacity and CO_2 sorption rate in the sorption enhanced reformer [35]; its input mass flow rate, $W_{s,0}$, is fixed according to the sorption capacity required by the methane reforming process. As far as the feeding gas is concerned, the input temperature is reached downstream of a preheating section, thanks to exchange of heat with the calciner output stream (≈ 900 °C); its fuel (methane) content is fixed with reference to the thermal input required by the calciner, to be provided by methane combustion; the carbon dioxide inlet flow allows to reach the operating fluidizing velocity.

The bundle of tubular OTM is made of 341 vertical tubes, 10 mm OD, all connected in parallel to allow air flow on the retentate side (i.e. inside the pipes) and sufficient oxygen permeation through their lateral walls.

The height of the bed of solids in the calciner before fluidization, H_0, and its diameter, d_{calci}, are fixed on the base of preliminary calculations about reasonable geometry and size of the OTM system; the bed cross section takes into account the reduction in surface area linked to the presence of tubular membranes.

Assuming convective plus axially dispersed flow for gas in the bubbles and in the emulsion phase, according to RTD tests on the cold model mentioned above, and a moving bed of solids travelling upward, the following molar balance equations are written for each component i (CO, CO_2, H_2O, CH_4, solid carbonate) in steady state conditions.

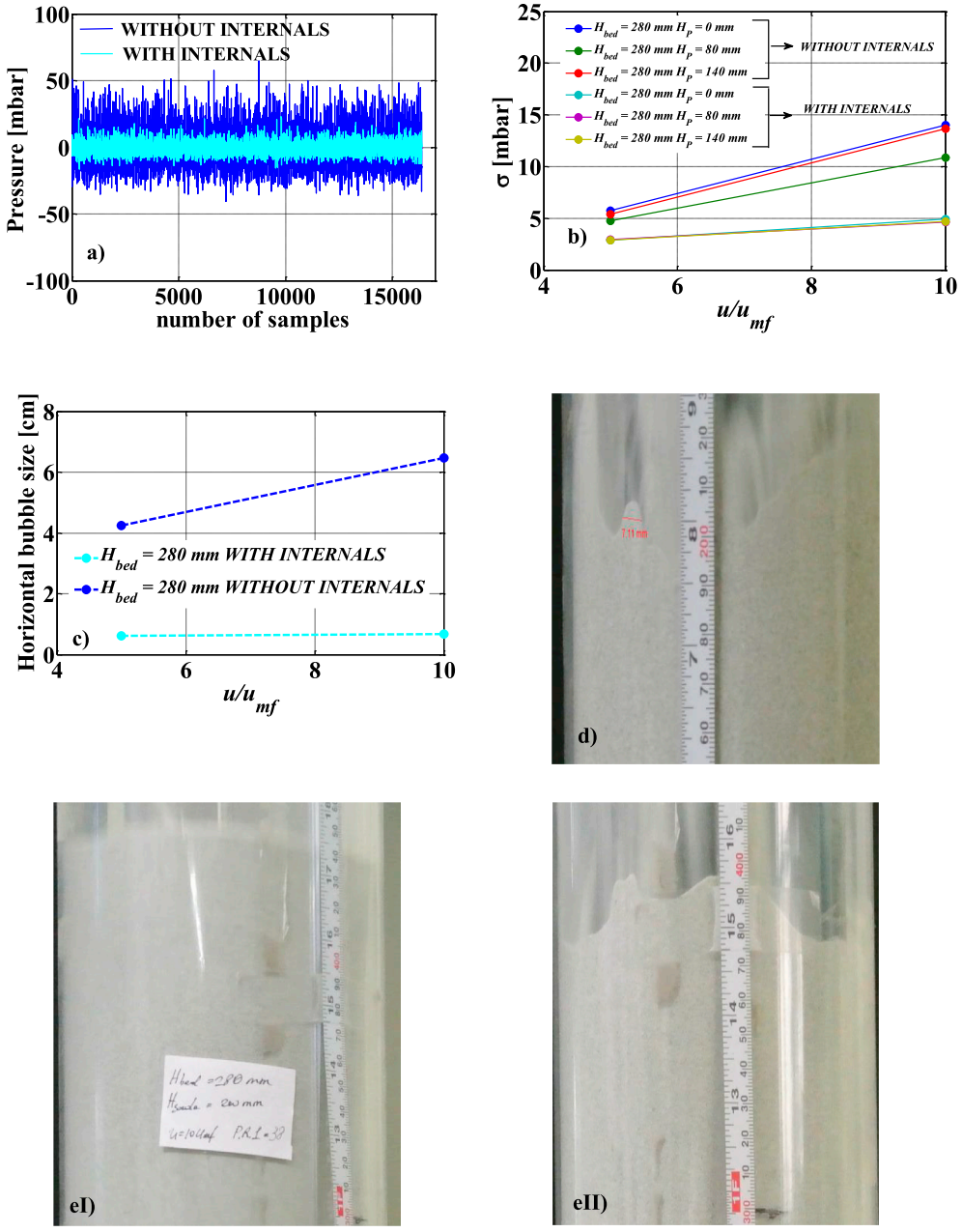

Fig. 5. Fluidization quality observed with the cold model with and without internals. a) amplitude of pressure fluctuations; b) standard deviation *vs* fluidization velocity; c) horizontal bubble size estimated at the bed surface by visual observations; d) the effect of the bundle of vertical rods on the reduction of bubble size (initial bed height = 153 mm and u/u_{mf} = 10); e) comparison of bubbling bed height (bubble hold-up inside the bed) without (I) and with (II) the bundle of vertical rods (initial bed height = 280 mm and u/u_{mf} = 10).

Bubble gas phase

$$D_R\frac{d^2C_{i,b}}{dz^2}-\frac{1}{S}\left(Q_b\frac{dC_{i,b}}{dz}+C_{i,b}\frac{dQ_b}{dz}\right)-K_{be,i}\frac{6\delta}{d_B}(C_{ib}-C_{ie})+\nu_i\delta\frac{N\pi d_{m,out}}{S_{bed}}J_{O2}\Big|_{i\equiv CH4,CO,H2O}=0 \quad (16)$$

where the stoichiometric coefficient ν_i, given by Eq. (6), is positive for combustion products and negative for methane.

The volumetric bubble flow rate changes with temperature and molar flow, according to the equation of state for ideal gas (the pressure drop through the fluidized bed is neglected):

$$Q_{b,z}=Q_{b,0}\frac{T_{g,z}}{T_{g,0}}\frac{F_{b,z}}{F_{b,0}};\quad \frac{Q_{b,0}}{T_{g,0}F_{b,0}}=\frac{R}{P};\quad \frac{dQ_b}{dz}=\left[F_{b,z}\frac{dT_g}{dz}+T_{g,z}\frac{dF_b}{dz}\right]\frac{R}{P} \quad (17)$$

$$\frac{dF_b}{dz}=\sum_i\nu_i\delta N\pi d_m J_{O2}+\boldsymbol{r_{calci/CBN}}(1-\delta)(1-\varepsilon_{mf})S_{bed}; \quad (18)$$

where:

$\boldsymbol{r_{calci/CBN}}=\boldsymbol{r_{calci}}$ *if* $C_{CO2}<C_{CO2,eq}$(see equation (9))
$\boldsymbol{r_{calci/CBN}}=-\boldsymbol{r_{CBN}}$ *if* $C_{CO2}\geq C_{CO2,eq}$(see equation (10))

$$C_{CO2,b}=\frac{F_{b,z}}{Q_{b,z}}-\sum_{i\equiv CH4,CO,H2O}C_{i,b} \quad (19)$$

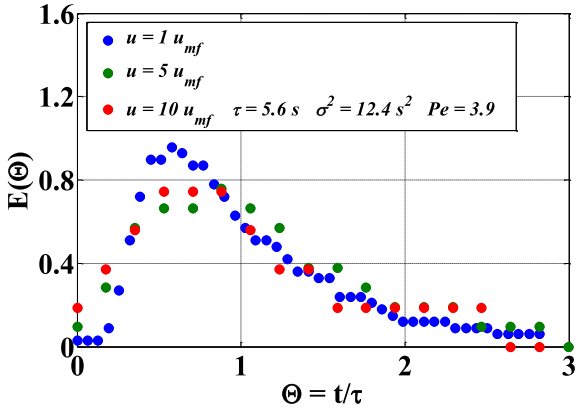

Fig. 6. Dimensionless characterization of gas phase RTD for the cold model operated at different fluidization velocities; estimate of the axial Péclet number for $u_0 = 10u_{mf}$

Table 4
Input parameters for the numerical simulation of the calciner reactor.

Operating conditions		Values
P	[atm]	1
$T_{g,0}$	[°C]	850, 750, 700
$T_{s,0}$	[°C]	650
$F_{CH4,0}$	[mol/s]	0.25
$F_{CO2,0}$	[mol/s]	1.33
OTM system		
N	[-]	341
$d_{m,out}$	[mm]	10.0
$d_{m,av}$	[mm]	9.6
H_{OTM}	[mm]	640, 740, 820
Calciner size		
H_0	[mm]	770
d_{calci}	[mm]	600
S_{bed}	[m^2]	0.26
Main input parameters values		
$u_{mf,calci}$ (900 °C)	[m/s]	0.06
ε_{mf}	[-]	0.4
$W_{s,0}$	[kg/s]	0.09
X_0	[-]	0.70
$\rho_{p,0}$	[kg/m^3]	1698
d_B	[mm]	28.9 ($d_{B,0}$), 57.8, 86.7
D_R	[m^2/s]	0.18

Emulsion gas phase

$$D_R\frac{d^2C_{i,e}}{dz^2} - \frac{1}{S_{bed}}\left(Q_e\frac{dC_{i,e}}{dz} + C_{i,b}\frac{dQ_e}{dz}\right) + K_{be,i}\frac{6\delta}{d_B}(C_{ib} - C_{ie}) + \nu_i(1-\delta)\frac{N\pi d_{m,out}}{S_{bed}}J_{O2}\Big|_{i\equiv CH4,CO,H2O} = 0 \quad (20)$$

$$\frac{dQ_e}{dz} = \left[F_{e,z}\frac{dT_g}{dz} + T_{g,z}\frac{dF_e}{dz}\right]\frac{R}{P};\quad \frac{dF_e}{dz} = \sum_i \nu_i(1-\delta)N\pi d_m J_{O2};\quad C_{CO2,e} = \frac{F_{e,z}}{Q_{e,z}} - \sum_{i\equiv CH4,CO,H2O} C_{i,e} \quad (21)$$

Gas interchange between bubbles and emulsion, per unit volume of the bed, is described by means of a transfer term appearing in the molar balance for each compound: the transfer coefficient, $K_{be,i}$, is estimated according to the method proposed by Kunii and Levenspiel [36]:

$$K_{be,i} = \frac{3}{4}\cdot u_{mf} + D_{i,CO2}{}^{1/2}\cdot\left(\frac{g}{d_B}\right)^{1/4} \quad (22)$$

Calcium carbonate solid phase

$$u_p N_{CaO}\frac{dX}{dz} = -\boldsymbol{r_{calci/CBN}}(1-\varepsilon_{mf})(1-\delta) \quad (23)$$

where u_p is defined in Eq. (14) with reference to solid mass flow rate and density in the entrance section, at the bottom of the bed; u_p is constant along the bed because particle volume doesn't change.

Boundary conditions:

Danckwerts boundary conditions are adopted both at the entrance and exit cross sections of the system [49]:

$$z = 0 \rightarrow F = F_0|_{b/e};\quad Q = Q_0|_{b/e};\quad F_{CH4,0} = \left(C_{CH4}Q - D_R\frac{dC_{CH4}}{dz}S_{bed}\right)\Big|_{0,b/e} \quad 0 = \left(C_iQ - D_R\frac{dC_i}{dz}S_{bed}\right)\Big|_{0,b/e,i\equiv CO,H2O};\quad X = X_0\quad z = H_{bed} \rightarrow \frac{dC_i}{dz} = 0 \quad (24)$$

Gas and solid enter the calciner reactor at different temperature, so two different energy balances are considered, although a numerical estimate (see Supplementary Material) shows that after a distance of the order of the average particle diameter the temperatures of both phases assume very close values.

A thermal conductivity term is omitted in the mechanism of energy transport in the bed of solids: numerical integration with the addition of such a term in Eq. (26) shows that the results, specifically the solid temperature profile along the bed, change very slightly, when compared with those obtained with the purely convective energy transport mechanism. In addition, the presence of a dense vertical packing system (the tubular membrane bundle) hinders back-mixing phenomena inside the bed. These are conservative assumptions, because the effective temperature profile in the bottom part of the bed might be somewhat steeper than that calculated by the model (Figs. 7 and 9), with a relative increase of OTM permeability and a reduced height of the reactor to get solid calcination.

Gas phase energy balance

$$F_g\cdot\overline{C_{p,g}}\cdot\frac{dT_g}{dz} = (1-\varepsilon_{mf})(1-\delta)\left[h_{gs}\frac{6}{d_p}(T_s - T_g) + \boldsymbol{r_{calci/CBN}}C_{p,CO2}(T_s - T_g)\right]S_{bed} - J_{O2}N\pi d_{m,out}\Delta H_{r1} - 0.04F_{CH4,0}\Delta H_{comb,CH4}/H_{bed} \quad (25)$$

Solid phase energy balance

$$W_s\cdot C_{p,s}\cdot\frac{dT_s}{dz} = (1-\varepsilon_{mf})(1-\delta)\left[h_{gs}\frac{6}{d_p}(T_g - T_s) + \boldsymbol{r_{calci/CBN}}C_{p,CO2}(T_g - T_s) - \boldsymbol{r_{calci/CBN}}\Delta H_{r2}\right]S_{bed} \quad (26)$$

Boundary conditions:

$$z = 0 \rightarrow T_g = T_{g,0};\quad T_s = T_{s,0} \quad (27)$$

The gas – particle heat transfer coefficient, h_{gs}, is estimated by means of the Gunn correlation [50]:

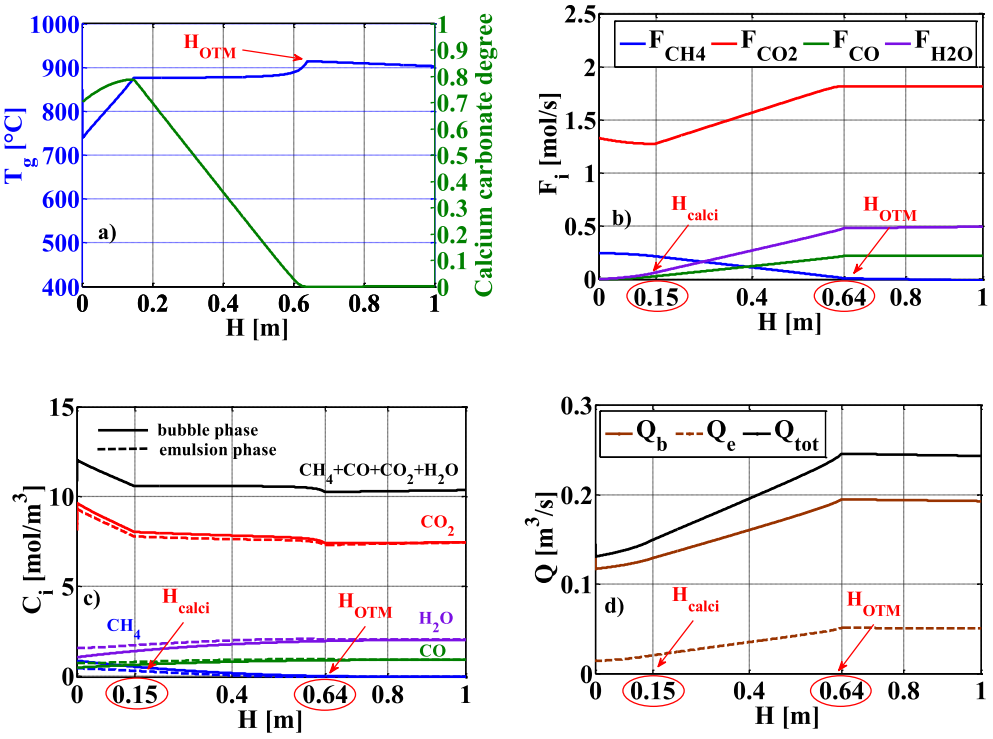

Fig. 7. Major trends *vs* bed height obtained in simulations ($T_{g,0}$ = 850 °C, X_0 = 70 %, H_{OTM} > bed height obtained in simulations = 0.64 m, $d_B = d_{B,0}$): (a) gas temperature and solid carbonation conversion; (b) molar flow rate of different gas compounds; (c) volumetric concentrations in the bubble and in the gas phase; (d) bubble-, emulsion- and overall volumetric gas flow rates.

$$Nu = (7 - 10\varepsilon_{mf} + 5\varepsilon_{mf}^2)\cdot(1 + 0.7Re^{0.2}\,Pr^{1/3}) + (1.33 - 2.4\varepsilon_{mf} + 1.2\varepsilon_{mf}^2)\cdot Re^{0.7}\,Pr^{1/3} \quad (28)$$

The heat capacities of both gas and solid chemical components are calculated by mean of correlations as functions of temperature [51].

4.1. Results of simulations

The above balance equations, together with boundary conditions, were integrated numerically utilizing function BVP5C of MATLAB® software. The BVP5C function uses a code that implements the four-stage Lobatto IIIa method to obtain the solution of the differential equations. This is a collocation formula and the collocation polynomial algorithm provides a C1-continuous solution with uniform fifth-order accuracy in [0,H]. In particular, the formula is implemented as an implicit Runge-Kutta routine, where the algebraic equations are solved directly [52]. The BVP5C function is able to estimate the true error, that between the exact solution of the original partial differential equations system and the numerical solution of the ordinary differential equations system. Thanks to this estimation, the function adapts the spatial discretization in order to keep the error lower than the tolerance declared by the user. For this reason, a sensitivity analysis was carried out varying the maximum relative and absolute error from $1{\cdot}10^{-1}$ to $1{\cdot}10^{-8}$, corresponding to an initial spatial discretization of $2{\cdot}10^{-4}$ m and $8{\cdot}10^{-6}$ m, respectively. The maximum absolute difference between corresponding concentration values evaluated at the different tolerance limits is in the order of $1{\cdot}10^{-5}$. The default values (relative error equal to $1{\cdot}10^{-3}$ and absolute error equal to $1{\cdot}10^{-6}$) were then used for the simulations to reduce the computational time, without losing accuracy of the results.

Parameter values reported in Table 4 were initially fixed as a result of preliminary guesses on the reactor sizing and operating conditions. Major results obtained with simulations are summarized in Fig. 7.

The gas temperature profile along the bed is shown in Fig. 7a, together with the progressive reduction of the calcium carbonation degree. It is worth noticing that, under the assumed operating conditions, the bed of solids is predicted to reach a fully calcined state at the top of the calciner, where the particulate solid is extracted to be circulated back to the SESMR reactor; the gas temperature first increases up to a level suitable for calcination and then keeps an almost constant value during the reaction process. The initial, abrupt decrease of T_g, from 850 °C to about 750 °C, is the result of the intense exchange of heat with the solid phase taking place there. The particle heating time when in contact with the hotter gas stream at the bottom of the calciner is estimated close to 1 s, corresponding to a distance of around 400 μm above the bottom of the bed [36]. (Calculation details are reported in the Supplementary Material).

Progressive methane combustion along the reactor with oxygen permeated through the OTM system allows reaching the desired gas and solid temperature: H_{calci} marks the end of this heating process and the start of the calcination process, just 0.15 m, i.e. about a quarter of the overall height of the membrane vertical bundle, H_{OTM}. The massive calcination process is completed just below H_{OTM}, fixed thanks to a preliminary dimensioning of the OTM system in terms of available permeation surface and oxygen permeation rate, J_{O2}, as a function of temperature.

J_{O2} increases exponentially with temperature (see Eqs. (4) and (5)), so that the heating step is affected by low oxygen permeability in the entrance region: in simulations, it is assumed that the membrane temperature is equal to T_g at each reactor height. As a result, it is important to guarantee a temperature level as high as possible in the entrance section of the reactor: this is partially obtained by upstream heating the gas entering the calciner, as mentioned above and discussed in the following model sensitivity analysis, and also helped by an initial, further carbonation of the incoming solid particles put into contact with a gas rich in carbon dioxide, at a temperature level below that needed for calcination, as evidenced by the numerical results shown in Fig. 7a. This exothermic process, already mentioned in section 2.2 and simulated by means of a reliable carbonation model (PGM), makes available an additional amount of heat compared to that produced by the combustion of methane, right in the bottom area of the calciner.

On the other hand, to avoid that gas (and solid) temperature increases above the level required by calcination, once it has been completed, it is crucial to choose the proper height for the OTM bundle, H_{OTM}, and/or methane input flow rate. In simulations, some heat losses from the calciner to the surroundings have been considered along the

height of the reactor, in the measure of 4 % of the heat produced by methane combustion; this assumption is considered satisfactory for pilot scale, well insulated equipment. This explains the slow decline in the temperature level appearing in Fig. 7a with reference to the upper part of the calciner, that above the tubular OTM bundle.

Temperature stability during calcination denotes that oxygen permeation is the step controlling the evolution of the particles de-carbonation process, via the heat input rate associated to methane combustion, which is essential to progress the endothermic calcination reaction and keep the temperature level above the threshold value assuring appreciable chemical kinetics.

Fig. 7b shows the evolution of molar flow rate of all gas compounds along the bed height, as predicted by the model. The reduction of CH_4 molar flow and increase of CO and H_2O, as a result of the combustion reaction with O_2, is moderate in the bottom part of the calciner, confirming the above discussion regarding oxygen permeation as a function of temperature.

Volumetric concentrations are reported in Fig. 7c: the overall gas molar density first decreases because of temperature increases (according to the ideal gas law) and then remains quite stable. For each component, very slight differences in concentration between bubble and emulsion phase are predicted, because bubbles are very small (see the sensitivity study below) assuring a relatively large specific surface area for interphase bubble-emulsion mole transfer. It is also noticeable the influence of axial dispersion on the concentration profile of the combustion products (mainly CO and H_2O, see Eqs. (16) and (20)), which are not present in the reactor input flow rate with a convective contribution.

The change in volumetric concentration and molar flow rate of all components have a clear effect on the profile of volumetric flow rate in the bubble and emulsion phase, respectively (Fig. 7d). In absolute terms, the increase of bubble flow *vs* bed height largely predominates due to the formation of endogenous bubbles when gaseous CO_2 is formed because of de-carbonation of solid particles. In the model, the most straightforward consequence is the increase of bubble fraction with superficial velocity, u, according to Eq. (15), progressively from about 23 % to about 30 % of the whole bed volume.

4.2. Model sensitivity analysis

Figs. 8 (a, b, c), 9 (a, b, c) and 10 show the sensitivity of simulations as a function of some model parameters and input conditions.

In Fig. 8 the influence of the equivalent bubble diameter (the diameter of a sphere with the same volume as that of the average bubble) on gas concentration profiles along the bed is shown. The simulations previously reported in Fig. 7 were obtained assuming $d_B = d_{B,O}$, i.e. equal to the spacing of pitch chosen for the vertical bundle of tubular OTMs, and in agreement with evidences gathered from the cold model about the existence of small bubbles predominantly confined between neighboring OTM pipes. However, those evidences also show that bubbles are generally quite elongated, with length substantially bigger that width. For this reason, it was decided to investigate the influence of increasing equivalent bubble diameter; the remaining model parameters keep the same values as that in Fig. 7. The comparison among trends shown in Fig. 8a, 8b and 8c, respectively, indicates that, for each component, the small concentration gap between bubble and emulsion phase at a given bed height is predicted to enlarge slightly as the bubble size increases, because the specific bubble surface becomes progressively smaller, and corresponding interphase molar flows are reduced. In none of the examined cases, however, the major parameters characterizing the calciner behavior, for example H_{calci}, are affected significantly.

On the other hand, Fig. 9 shows that more important changes are linked to differences in the input temperature of the gas stream, $T_{g,0}$. As it was mentioned above, the solid input temperature ($T_{s,0}$ = 650 °C) is fixed by the operating temperature of the reforming and CO_2 sorption reactor, so that it can hardly be changed, instead the input gas temperature level could be chosen as a result of heat recovery strategies from process streams. Fig. 9a and b show that temperature strongly affects oxygen permeation through the OTM surface and consequently sensible heat released by methane combustion, so that the whole temperature profile along the calciner undergoes considerable variations. This means that temperature levels assuring substantial rate of calcination may be reached at increasing height in the calciner, and in some cases a complete calcination of solid particles could become problematic (Fig. 9c).

In a recent paper on CFD simulation of a SESMR fluidized bed reactor at pilot scale [25] we did show the influence of the degree of sorbent calcination fed to the reformer on the estimated performance of the combined methane reforming and CO_2 capture process. The numerical results of the CFD model showed that with fully calcined particles and at every investigated superficial velocity, a composition close to sorption enhanced chemical equilibrium was obtained; when the initial calcination degree is reduced, the hydrogen yield is also reduced, although higher than that corresponding to plain SMR equilibrium. As a result, complete calcination is a desirable target, even if not a strict requirement.

Finally, Fig. 10 shows the contribution to the temperature profile in the calciner provided by the exothermic, initial solid carbonation, which becomes increasingly important as the inlet temperature is more substantially reduced: simulation results reported in Fig. 10 show clearly that, without this contribution, temperature (and consequently oxygen permeability through the OTM) would have a profile considerably less steep in the bottom part of the calciner, so that calcination would require comparatively larger OTM surface (and bed height): as shown in Fig. 10, the required membrane surface area would increase by 15 % with a gas input temperature of 850 °C. Additional simulations indicate a corresponding increase of 35 % when the inlet gas

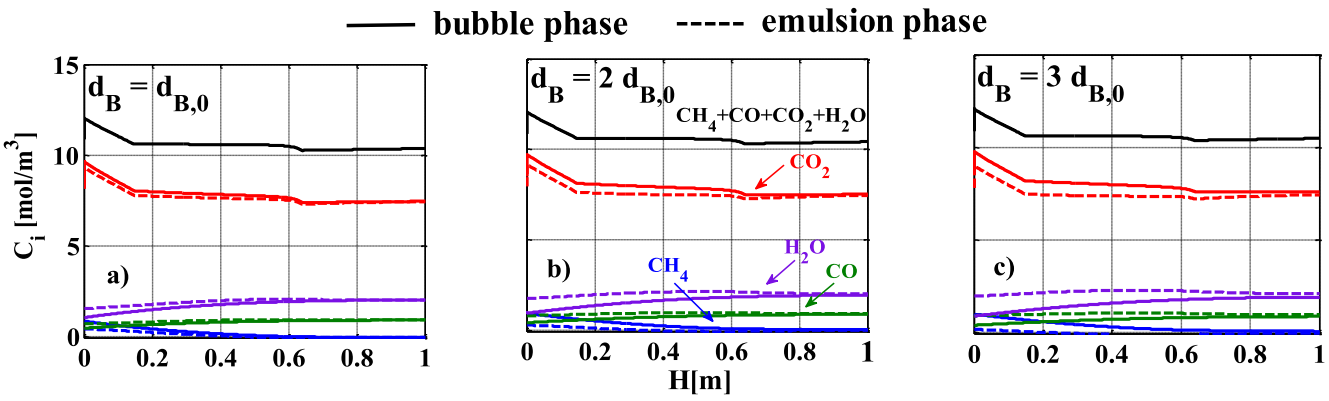

Fig. 8. Volumetric concentrations along the bed height as functions of the equivalent bubble size, d_B; all remaining model parameters are those utilized in Fig. 7.

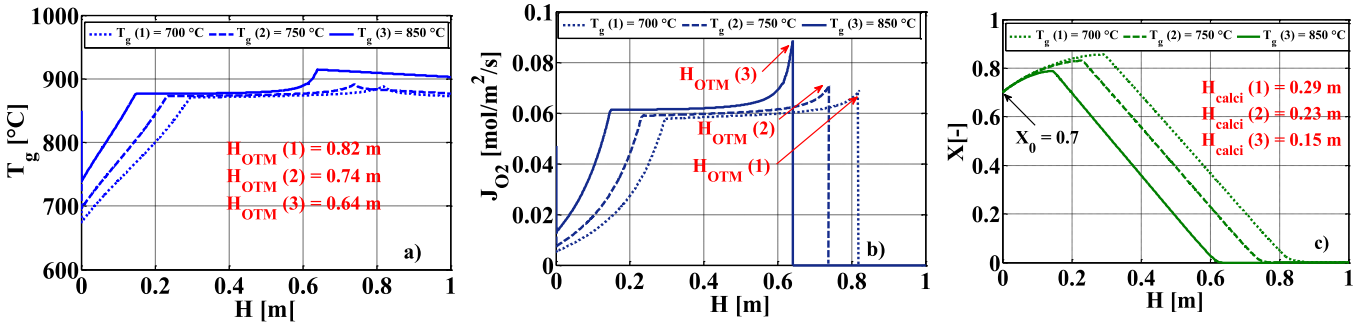

Fig. 9. (a) gas temperature, T_g, (b) oxygen flux, J_{O2}, and (c) solid carbonation degree, X, along the bed height, for different values of inlet gas temperature, $T_{g,0}$; the height of the OTM vertical bundle is adjusted to obtain complete solid calcination in each examined case.

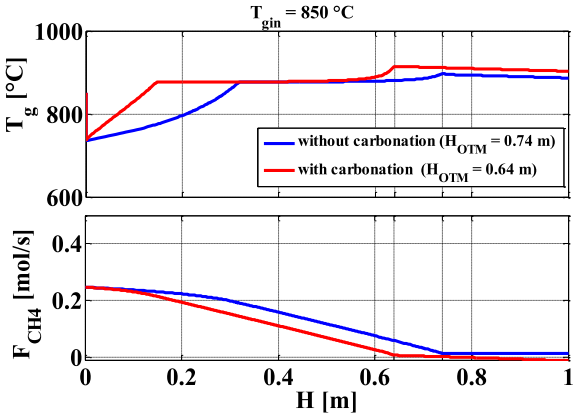

Fig. 10. Temperature and methane molar flow rate along the calciner fluidized bed, under conditions examined in Fig. 7 (red lines) and assuming negligible solid carbonation at the bottom of the calciner (blue lines).

temperature is equal to 750 °C, and for lower gas inlet temperature it would become quite difficult to reach reasonable membrane permeability without the contribution of exothermic solid carbonation at the bottom of the reactor. On the other hand, the numerical results reported in Fig. 10 clearly show that the required, overall methane consumption would not change, as expected. Once more, membrane oxygen permeation is identified as the limiting factor for a smooth and efficient operation of the calcination reactor.

5. Conclusions

This work addresses the regeneration step of CaO-based sorbents utilized cyclically to capture CO_2 in sorption enhanced steam reforming processes, like SESMR, which are developed to increase efficiency, separate carbon dioxide and reduce costs of traditional SMR. Calcination is an endothermic process and needs to be performed at high temperature (≈ 900 °C) even at atmospheric pressure, if a pure CO_2 stream is desired for sequestration and/or utilization. Providing heat under those conditions is not an easy task: to allow a direct supply of heat inside the reactor, oxyfuel combustion of methane is suggested utilizing Oxygen Transport Membranes (OTMs), a potentially convenient means of air fractionation at high temperatures, especially in case of small scale applications.

Previous studies allowed to characterize oxygen permeability for tubular OTMs and to validate an Arrhenius-type model for the oxygen permeation flux as a function of temperature. Moreover, in this study the calcination kinetics of a dolomite sample was investigated by means of TGA experimental tests, which helped defining the kinetic constant to be inserted in a rate expression taken from the literature. Finally, realization and operation of a cold model, geometrically and dynamically similar to the calciner, allowed to highlight the hydrodynamic fluidization quality and gas residence time distribution when a vertical bundle of rods mimicking OTM pipes is inserted in a cylindrical bed of powder.

The above experimental evidences were utilized to propose a simulation model to predict numerically the behavior of the calciner, made of molar balances for each chemical species in the bubble, emulsion and solid phase, and energy balances for gas and solid flowing along the reactor. Reference is made to the ZECOMIX SESMR pilot plant (5 kmol/h of H_2).

The numerical results show that in the examined case is indeed feasible the complete calcination of the mass flow rate of dolomite required by the SESMR reactor, utilizing the OTM surface immersed in the fluidized bed to burn methane in the oxy-fuel mode and provide the necessary input of heat. Oxygen permeability through the membrane is a strong function of temperature, so that the extent of calcination obtainable is related to the temperature level at the inlet of the calciner; as a result, the oxygen transfer rate is the key kinetic step affecting size and operating conditions of the calciner. Simulations show the important contribution to enhance temperature profile (and oxygen permeation) in the bottom region of the calciner offered by further carbonation of the inlet solid particles, which reduces the overall height of the OTM bundle and of the fluidized bed, without increasing the thermal load provided by methane oxy-combustion.

Acknowledgment

This work was carried out under the Italian national research program “Ricerca di Sistema Elettrico”. The authors wish to thank the Italian Ministry of Economic Development and ENEA - Italian National Agency for New Technologies, Energy and Sustainable Economic Development for funding.

Appendix A. Supplementary data

Supplementary data to this article can be found online at https://doi.org/10.1016/j.cej.2018.11.021.

References

[1] H. McJeon, J. Edmonds, N. Bauer, L. Clarke, B. Fisher, B.P. Flannery, J. Hilaire, V. Krey, G. Marangoni, R. Mi, K. Riahi, H. Rogner, M. Tavoni, Limited impact on decadal-scale climate change from increased use of natural gas, Nature 514 (2014) 482–485.
[2] International Energy Agency, Are We Entering a Golden Age of Gas? (IEA Report, 2011), http://www.worldenergyoutlook.org/media/weowebsite/2011/WEO2011_GoldenAgeofGasReport.pdf (accessed 4.05.18).
[3] D. Littell, Natural gas: bridge or wall in transition to low-carbon economy? Nat. Gas Electr. 33 (2017) 1–8.
[4] Y. Qin, F. Tong, G. Yang, D.L. Mauzerall, Challenges of using natural gas as a carbon mitigation option in China, Energy Policy 117 (2018) 457–462.
[5] C. McGlade, S. Pye, P. Ekins, M. Bradshaw, J. Watson, The future role of natural gas in the UK: A bridge to nowhere? Energy Policy 113 (2018) 454–465.
[6] N.L. Panwar, S.C. Kaushik, Surendra Kothari, Role of renewable energy sources in environmental protection: a review, Renew. Sust. Energ. Rev. 15 (2011)

1513–1524.
[7] O. Ellabban, H. Abu-Rub, F. Blaabjerg, Renewable energy resources: current status, future prospects and their enabling technology, Renew. Sust. Energ. Rev. 39 (2014) 748–764.
[8] J. Lipp, Lessons for effective renewable electricity policy from Denmark, Germany and the United Kingdom, Energ. Policy 35 (2007) 5481–5495.
[9] International Energy Outlook 2017 Overview, Report Number: DOE/EIA-0484 (2017) https://www.eia.gov/outlooks/ieo/ (accessed 4.05.18.).
[10] T. da Silva Veras, T.S. Mozer, D. da Costa, Rubim Messeder dos Santos, A. da Silva César Hydrogen: trends, production and characterization of the main process worldwide, Int. J. Hydrogen Energy 42 (2017) 2018–2033.
[11] J.D. Holladay, J. Hu, D.L. King, Y. Wang, An overview of hydrogen production technologies, Catal. Today 139 (2009) 244–260.
[12] S.A. Bhat, J. Sadhukhan, Process intensification aspects for steam methane reforming: an overview, AIChE J. 55 (2009) 408–422.
[13] B. Dou, C. Wang, Y. Song, H. Chen, B. Jiang, M. Yang, Y. Xu, Solid sorbents for in-situ CO_2 removal during sorption-enhanced steam reforming process: a review, Renew. Sust. Energ. Rev. 53 (2016) 536–546.
[14] M.S. Yancheshmeh, H.R. Radfarnia, M.C. Iliuta, High temperature CO_2 sorbents and their application for hydrogen production by sorption enhanced steam reforming process, Chem. Eng. J. 283 (2016) 420–444.
[15] C. Hawthorne, H. Dieter, A. Bidwe, A. Schuster, G. Scheffknecht, S. Unterberger, M. Käß, CO_2 capture with CaO in a 200 kW_{th} dual fluidized bed pilot plant, Enrgy. Proced. 4 (2011) 441–448.
[16] K. Johnsen, H.J. Ryu, J.R. Grace, C.J. Lim, Sorption-enhanced steam reforming of methane in a fluidized bed reactor with dolomite as CO_2-acceptor, Chem. Eng. Sci. 61 (2006) 1195–1202.
[17] M.C. Romano, E.N. Cassotti, P. Chiesa, J. Meyer, J. Mastin, Application of the sorption enhanced-steam reforming process in combined cycle-based power plants, Energy Proced. 4 (2011) 1125–1132.
[18] V. Spallina, A. Shams, A. Battistella, F. Gallucci, M. van, Sint Annaland, chemical looping technologies for H_2 production with CO_2 capture: thermodynamic assessment and economic comparison, Energy Proced. 114 (2017) 419–428.
[19] I. Martínez, M.C. Romano, P. Chiesa, G. Grasa, R. Murillo, Hydrogen production through sorption enhanced steam reforming of natural gas: thermodynamic plant assessment, Int. J. Hydrogen Energy 38 (2013) 15180–15199.
[20] L. Barelli, G. Bidini, F. Gallorini, S. Servili, Hydrogen production through sorption-enhanced steam methane reforming and membrane technology: a review, Energy 33 (2008) 554–570.
[21] S.D. Angeli, G. Monteleone, A. Giaconia, A.A. Lemonidou, State-of-the-art catalysts for CH_4 steam reforming at low temperature, Int. J. Hydrogen Energy 39 (2014) 1979–1997.
[22] U. Sikander, S. Sufian, M.A. Salam, A review of hydrotalcite based catalysts for hydrogen production systems, Int. J. Hydrogen Energy 42 (2017) 19851–19868.
[23] S.A. Salaudeen, B. Acharya, A. Dutta, CaO-based CO_2 sorbents: a review on screening, enhancement, cyclic stability, regeneration and kinetics modelling, J. CO_2 Util. 23 (2018) 179–199.
[24] M. Voldsund, K. Jordal, R. Anantharaman, Hydrogen production with CO_2 capture, Int. J. Hydrogen Energy 41 (2016) 4969–4992.
[25] A. Di Carlo, I. Aloisi, N. Jand, S. Stendardo, P.U. Foscolo, Sorption enhanced steam methane reforming on catalyst-sorbent bifunctional particles: A CFD fluidized bed reactor model, Chem. Eng. Sci. 173 (2017) 428–442.
[26] H. Pawlak-Kruczek, M. Baranowski, Effectiveness of CO_2 Capture by calcium looping with regenerated calcium sorbents – last step calcination, Energy Proced. 105 (2017) 4499–4512.
[27] B.R. Stanmore, P. Gilot, Review-calcination and carbonation of limestone during thermal cycling for CO2 sequestration, Fuel. Process. Technol. 86 (2005) 1707–1743.
[28] J. Meyer, J. Mastin, Tor-K. Bjørnebøle, T. Ryberg, N. Eldrup, Techno-economical study of the zero emission gas power concept, Enrgy. Proced. 4 (2011) 1949–1956.
[29] T. Antonini, K. Gallucci, V. Anzoletti, S. Stendardo, P.U. Foscolo, Oxygen transport by ionic membranes: correlation of permeation data and prediction of char burning in a membrane-assisted biomass gasification process, Chem. Eng. Process.: Process Intensif. 94 (2015) 39–52.
[30] S. Stendardo, P.U. Foscolo, M. Nobili, S. Scaccia, High quality syngas production via steam-oxygen blown bubbling fluidised bed gasifier, Energy 103 (2016) 697–708.
[31] S. Scaccia, S. Stendardo, G. Vanga, L. Pagliari, S. Cassani, M. Nobili, G. Messina, A. Assettati, G. Guidarelli, S. Attanasi, C. Stringola, A. Grasso, I. Cassani, A. Calabró, P.U. Foscolo, The Italian ZECOMIX platform: CO_2 capture on calcined dolomite in fluidized bed carbonator unit, Nat. Resour. 5 (2014) 433–441.
[32] Y.-S. Zheng, Y.-A. Zhu, Y. Li, X.-G. Zhou, W.-K. Yuan, Mechanism of Oxygen Transport in La-Based Perovskites from First Principles, in: ISCRE 25: 25th Int. Conf. Chem. React. Eng. " Eng. Chem. Transform. by Bridg. Sci. Technol. ", Florence, Italy, May 20–23, 2018.
[33] R. Di Felice, S. Rapagna, P.U. Foscolo, L.G. Gibilaro, Cold modelling studies of fluidised bed reactors, Chem. Eng. Sci. 47 (1992) 2233–2238.
[34] F. Fang, Z.S. Li, N.S. Cai, Experiment and modeling of CO_2 capture from flue gases at high temperature in a fluidized bed reactor with Ca-based sorbents, Energy Fuels 23 (2009) 207–216.
[35] I. Aloisi, A. Di Giuliano, A. Di Carlo, P.U. Foscolo, C. Courson, K. Gallucci, Sorption enhanced catalytic steam methane reforming: experimental data and simulations describing the behaviour of bi-functional particles, Chem. Eng. J. 314 (2017) 570–582.
[36] D. Kunii, O. Levenspiel, Fluidization Engineering, Second ed., Butterworth-Heinemann, Boston, 1991.
[37] T. Antonini, P.U. Foscolo, K. Gallucci, S. Stendardo, Influence of temperature on oxygen permeation through ion transport membrane to feed a biomass gasifier, J. Phys. Conf. Ser. 655 (2015) 1–10.
[38] J.R. Arthur, Reaction between carbon and oxygen, T. Faraday Soc. 47 (1950) 164–178.
[39] L. Di Felice, V. Middelkoop, V. Anzoletti, F. Snijkers, M. van Sint Annaland, F. Gallucci, New high temperature sealing technique and permeability data for hollow fiber BSCF perovskite membranes, Chem. Eng. Process. Process Intensif. 107 (2016) 206–219.
[40] S. Stendardo, P.U. Foscolo, Carbon dioxide capture with dolomite: a model for gas-solid reaction within the grains of a particulate sorbent, Chem. Eng. Sci. 64 (2009) 2343–2352.
[41] I. Aloisi, N. Jand, S. Stendardo, P.U. Foscolo, Hydrogen by sorption enhanced methane reforming: a grain model to study the behavior of bi-functional sorbent-catalyst particles, Chem. Eng. Sci. 149 (2016) 22–34.
[42] S.K. Bhatia, D.D. Perlmutter, Effect of the product layer on the kinetics of the CO2-lime reaction, AIChE J. 29 (1983) 79–86.
[43] L.R. Glicksman, M. Hyre, K. Woloshun, Simplified scaling relationships for fluidized beds, Powder Technol. 77 (1993) 177–199.
[44] D. Geldart, Types of gas fluidization, Powder Technol. 7 (1973) 285–292.
[45] L.G. Gibilaro, Fluidization-Dynamics, first ed., Butterworth - Heinemann, Oxford, 2001.
[46] A. Helmi, I. Campos Velarde, F. Gallucci, M. van, Sint Annaland, Hydrodynamics of dense gas-solid fluidized beds with immersed vertical membranes using an endoscopic-laser PIV/DIA technique, Chem. Eng. Sci. 182 (2018) 146–161.
[47] M. Fiorentino, A. Marzocchella, P. Salatino, Segregation of fuel particles and volatile matter during devolatilization in a fluidized bed reactor - II. experimental, Chem. Eng. Sci. 52 (1997) 1893–1908.
[48] G. Bruni, R. Solimene, A. Marzocchella, P. Salatino, J.G. Yates, P. Lettieri, M. Fiorentino, Self-segregation of high-volatile fuel particles during devolatilization in a fluidized bed reactor, Powder Technol. 128 (2002) 11–21.
[49] H.S. Fogler, Elements of Chemical Reaction Engineering, fourth ed., Prentice Hall International, 2006.
[50] D.J. Gunn, Transfer of heat or mass to particles in fixed and fluidised bed, Int. J. Heat Mass Transfer 21 (1978) 467–476.
[51] R.H. Perry, D.W. Green, Perry's Chemical Engineers' Handbook, seven ed., McGraw-Hill, 1999.
[52] J. Kierzenka, L.F. Shampine, A BVP solver that controls residual and error, J. Numer. Anal. Ind. Appl. Math. 3 (2008) 27–41.